Biomaterials and Biomechanics in Bioengineering, *Vol. 2, No. 2 (2015) 71-84*
(Formerly, Biomaterials and Biomedical Engineering)
DOI: http://dx.doi.org/10.12989/bme.2015.2.2.071

A novel low-profile flow sensor for monitoring of hemodynamics in cerebral aneurysm

Yanfei Chen[1], Brian T. Jankowitz[2], Sung Kwon Cho[3], Woon-Hong Yeo[4] and Youngjae Chun[*1,5]

[1]*Department of Industrial Engineering, University of Pittsburgh, Pittsburgh, PA 15261, USA*
[2]*Department of Neurological Surgery, University of Pittsburgh Medical Center, Pittsburgh, PA 15213, USA*
[3]*Department of Mechanical Engineering and Materials Science, University of Pittsburgh, Pittsburgh, PA 15261, USA*
[4]*Department of Mechanical and Nuclear Engineering, Center for Rehabilitation Science and Engineering, Virginia Commonwealth University, Richmond, VA 23284, USA*
[5]*Department of Bioengineering, University of Pittsburgh, Pittsburgh, PA 15261, USA*

(Received March 14, 2015, Revised April 22, 2015, Accepted April 25, 2015)

Abstract. A low-profile flow sensor has been designed, fabricated, and characterized to demonstrate the feasibility for monitoring hemodynamics in cerebral aneurysm. The prototype device is composed of three micro-membranes (500-μm-thick polyurethane film with 6-μm-thick layers of nitinol above and below). A novel super-hydrophilic surface treatment offers excellent hemocompatibility for the thin nitinol electrode. A computational study of the deformable mechanics optimizes the design of the flow sensor and the analysis of computational fluid dynamics estimates the flow and pressure profiles within the simulated aneurysm sac. Experimental studies demonstrate the feasibility of the device to monitor intra-aneurysmal hemodynamics in a blood vessel. The mechanical compression test shows the linear relationship between the applied force and the measured capacitance change. Analytical calculation of the resonant frequency shift due to the compression force agrees well with the experimental results. The results have the potential to address important unmet needs in wireless monitoring of intra-aneurysm hemodynamic quiescence.

Keywords: cerebral aneurysm; flow sensor; thin film nitinol; capacitance; finite element modeling

1. Introduction

Cerebral aneurysm is a cerebrovascular disorder that is caused by the local ballooning in the blood vessels and the rupture of the aneurysm will cause serious complications, including hemorrhagic stroke, permanent nerve damage, or death. The prevalence of unruptured aneurysm varied considerably: 0.4% and 3.6% (for retro- and prospective autopsy studies) and 3.7% and 6% (for retro- and prospective angiography studies) (Wardlaw *et al*. 2000). The overall prevalence of unruptured aneurysm for people without comorbidity was 2.3% (Rinkel *et al*. 1998) and the

*Corresponding author, Professor, E-mail: yjchun@pitt.edu

 ISSN: 2288-3738 (Print), 2288-3746 (Online)

prevalence was higher for older women (Vlak *et al*. 2011). The presence of an unruptured aneurysm represents the potential risk and the aneurysm rupture leads to subarachnoid hemorrhage. An estimated 6.8 million Americans ≥20 years of age having had a stroke from 2006 to 2010 and the overall stroke prevalence during this period is estimated 2.8% (Go *et al*. 2013). The approximate rupture rate for unruptured aneurysms is 1.1% per year based on a long-term follow-up study. (Juvela *et al*. 2013). Current treatments of cerebral aneurysm involve surgical procedure and endovascular embolization. For the surgical procedure, clip integration is used to protect against the rupture. However, the assessed risk of morbidity associated with the clipping of unruptured aneurysms was reported as high as 15.7% (Brisman *et al*. 2006). Therefore, coiling has replaced clipping as a common procedure nowadays and the risks were reduced by 7.4% (Molyneux *et al*. 2005). While endovascular embolization is less invasive and carries a lower treatment risk, the cure rates lag behind those of clipping, primarily due to a significant rate of post-operative recanalization or regrowth due to persistent blood flow into the aneurysm in up to 38% of patients (Raymond *et al*. 2003). It is necessary to monitor the aneurysm until intra-aneurysmal flow is reduced enough to allow endothelialization or healing of the aneurysm neck, effectively sealing the pouch and eliminating any blood flow into the aneurysm.

High-quality catheter angiography is generally employed to evaluate subarachnoid hemorrhage for unruptured aneurysms. But angiography examination is qualitative and fails to disclose an aneurysm in 10 to 20 percent of cases of subarachnoid hemorrhage (Brisman *et al*. 2006). Another approach to monitor the aneurysm is pressure sensing. Both the direct intra-aneurysmal sac pressure measurement using tip-pressure sensors and wireless pressure sensing for endovascular aneurysm repair has been reported (Dias *et al*. 2004, Ellozy *et al*. 2004, Ohki *et al*. 2007). However, these sensors are not sufficiently flexible for use in intracranial endovascular procedures, which typically require a 1.7 Fr micro-delivery catheter (i.e., OD=0.56 mm). Also the recent studies have confirmed that the intra-aneurysm pressure is not significantly changed after the coil placement (Boecher *et al*. 2000, Canton *et al*. 2005, Sorteberg *et al*. 2001, Lam *et al*. 2013, Groden *et al*. 2001), which means the pressure sensor is not suitable for monitoring intra-aneurysm hemodynamic quiescence.

Therefore, there exists a great need for a device that enables monitoring of the intracranial aneurysm since the aneurysmal inflow that enters through the neck of aneurysm is significantly reduced after the coiling (Morales *et al*. 2010, Babiker *et al*. 2010). In this paper, we introduce a low-profile flow sensor to monitor intra-aneurysmal hemodynamics in an *in vitro* testing. Computational study determines the optimal design of a device and experimental study with the microfabricated device demonstrates the device functionality by measuring capacitance and resonant frequency shift according to an applied compression force.

2. Theory

Our idea of flow sensor is to adopt the parallel plate capacitor structure, i.e., a thin dielectric elastomer layer (e.g., polydimethylsiloxane and polyurethane) sandwiched between two thin metallic layers (e.g., TFN) and the concept of design is shown in Fig. 1(a). The sensor will be fully embedded in a pre-existing commercial aneurysm coil and a *de novo* style wound nitinol cage will be surrounded in order to protect the sensor from the external force during the coil deployment procedure. Such an approach will allow for a large degree of compactness and a greatly reduced sensor complexity. The theoretical equation for capacitance of parallel plate capacitor is given by

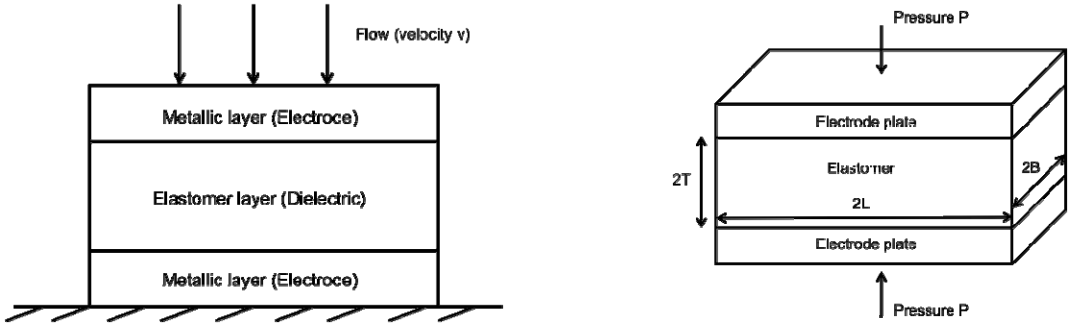

(a) Parallel plate capacitor (b) Compression with applied pressure

Fig. 1 Concept of the flow sensor

$$C = \frac{\varepsilon_r \varepsilon_0 A}{d} \tag{1}$$

where ε_0 is the permittivity of free space (8.85×10^{-12} F/m), ε_r is the relative dielectric constant of the polymer, A is the area of the metallic plate and d is the distance between these two plates. The capacitance will be increased if the distance between two plates is decreased due to compression.

2.1 Capacitance

For a rectangular layer of an incompressible, homogeneous elastomer that is bonded with rigid plates on both sides shown in Fig. 1(b), the relationship between an applied pressure, *P*, on two electrode plates and the resultant strain, *e*, can be expressed as (Kenichi *et al*. 2008)

$$P = \frac{EC}{2}\left(S^2 - S_0^2\right) - E\left[1 + \frac{1}{3}\left(\frac{B^2 - L^2}{B^2 + L^2}\right)^2\right]\log(1-e) \tag{2}$$

where E is the Young's modulus of the elastomer, 2*L* and 2*B* are the length and width of the rectangle layer, respectively, *C* is a constant given by

$$C = \frac{4}{3} + \frac{B}{L}\left(2 - \frac{11B}{10L}\right) \tag{3}$$

S is a geometric parameter called shape factor and is given by

$$S = \frac{BL}{2(L+B)t} = \frac{S_0}{1-e} \tag{4}$$

where 2*t* is the resultant thickness of the layer upon the compression and S_0 is the original shape factor with the initial thickness (2*T*) before the compression. The strain can be expressed as

$$e = \frac{2T - 2t}{2T} = \frac{\Delta T}{T} \tag{5}$$

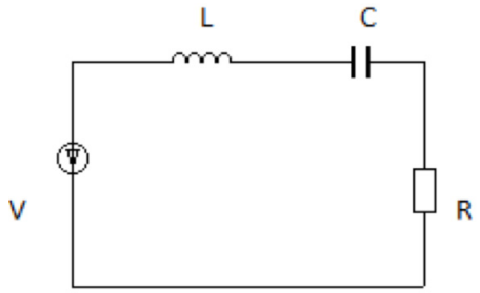

Fig. 2 Circuit diagram for RF measurement

Therefore, the capacitance change can be determined by

$$\Delta C = C - C_0 = \frac{\varepsilon_0 \varepsilon_r \left(4BL\Delta t\right)}{Tt} \approx C_0 e \propto \frac{\Delta T}{T^2} \tag{6}$$

Here, we assumed that $\Delta T \ll T$ and ΔB, $\Delta L \approx 0$ for simplicity. Therefore, the capacitance change is proportional to the thickness change over the square of the original thickness if the thickness change in response to compression is small compared to the original thickness. In this case, we can calculate this value under compression to evaluate the sensitivity of the sensors and our goal is to maximize the capacitance change with applied compression force.

2.2 Resonant frequency (RF)

The change of capacitance in response to flow compression will be transmitted via RF shifts of an internal LC circuit (sensor part) and detected in an external read-out circuit. In order to measure the RF shifts due to the capacitance change, the RF measurement circuit shown in Fig. 2 is built. In this circuit, C is the capacitor of the flow sensor. L and R are the inductor and resistor for constructing the measurement circuit. The input is supplied by a sine wave alternating current (AC) voltage and the output voltage on the resistor can be calculated as

$$\tilde{V}_{out} = \frac{R}{j\omega L + \frac{1}{j\omega C} + R} \tilde{V}_{in} \tag{7}$$

At resonant frequency of the circuit, which is determined by

$$f = \frac{1}{2\pi\sqrt{LC}} \tag{8}$$

The output voltage peak will be maximal and equal to the input voltage. Therefore, the RF can be measured by monitoring the output voltage with sweeping frequency in input voltage.

2.3 Computational fluid dynamics (CFD) analysis

The dynamic pressure P generated by the liquid flow in a tube is defined as

$$P = \frac{1}{2}\rho v^2 \tag{9}$$

where ρ is the density of the liquid flow and v is the velocity of the liquid flow. Since the elastomer layer is deformed by the pressure generated with the incoming flow, and the magnitude of deformation is proportional to the pressure from section 2.1, we need to assess the flow patterns in the aneurysm to optimize the sensor location within the aneurysm sac. We developed an aneurysm model with parent vessel to calculate the flow velocity and pressure distributions with defined boundary conditions including inlet velocity and outlet pressure.

3. Materials and methods

3.1 Materials for a prototype device

The sensor included an elastomer, dielectric layer composed of a low modulus (~1MPa) and biocompatible (Szycher 2012). The TFN was served as an electrode in the parallel capacitor structure. The TFN is a well-known biocompatible and hemocompatible material (details in the section 3.2). To make a prototype flow sensor, polyurethane parts A, B and C (74-30 series, Polytek, PA) were mixed together with the ratio of 1:1:1 and then poured in-between two TFN sheets. The device was cured for 24 hours at room temperature and two thin copper wires (36 AWG, Artistic Wire) were connected on the TFN plates for electrical connection.

3.2 Hemocompatibility of TFN

This study investigated the hemocompatibility of the TFN through surface treatment. While nitinol is a well-known biocompatible material, the thrombotic complications of nitinol frequently occur when it is used for vascular implants in small arteries. Two important factors of thrombosis are wettability and surface charge of a material. It is known that native blood vessels are negatively charged and hydrophilic, which has been postulated to decrease the attachment of blood products. By following the surface coating approach (Chun *et al*. 2009), the TFN was treated to achieve super hydrophilicity. Fig. 3(a) shows that less than 5 degree wetting angle (i.e., super-hydrophilic) is achieved after 15 hour-long treatment. Surface treated TFN samples (Fig. 3(b)) demonstrated no significant platelet adhesion (0-3 per mm^2) and no platelet aggregation ($p<0.01$) after 180 min of platelet contact, while the expanded polytetrafluoroethylene (ePTFE) samples showed evidence of dense platelet aggregation of more than 100 platelets per mm^2 (Tulloch *et al*. 2011). This study confirmed that the surface treatment of the nitinol material increased surface hydrophilicity and also significantly reduced platelet adhesion, which will reduce or eliminate thrombosis for TFN based indwelling devices.

3.3 Experimental setup

Fig. 4(a) shows an experimental setup for a mechanical compression test to evaluate the functionality of a prototype device. A fabricated capacitive sensor was placed between two plastic plates to achieve isolation and we approximated the flow velocity related pressure with the compression force generated by the spring. The compression force was gradually increased by

elevating the translation stage to deform the spring upward and the corresponding compression force was measured by a load cell (LSB200, Futek, CA) under the sensor. The change of capacitance was measured by an LCR meter (PXI 4072, National Instruments, TX) with copper wired connection probes and recorded using LabVIEW SignalExpress (National Instruments, TX).

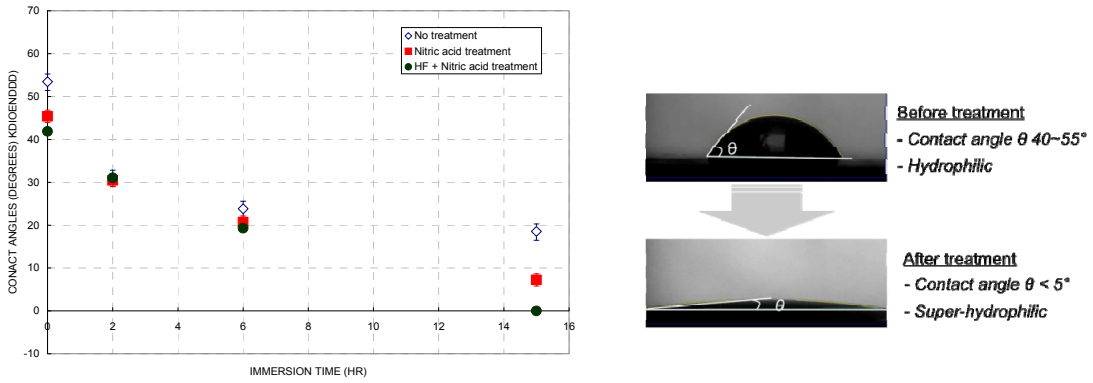

(a) Variation of the contact angle due to the surface treatment

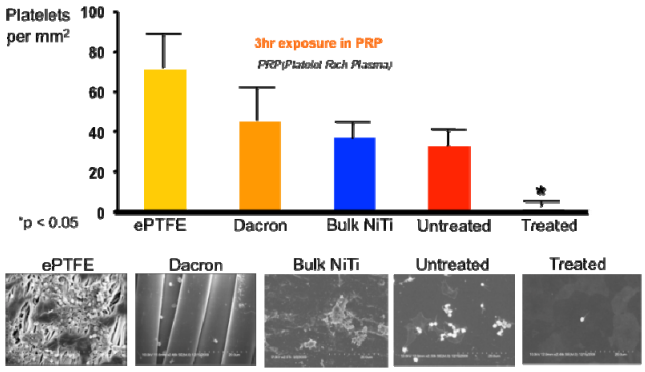

(b) Platelet adhesion per unit area of a material after contacting with platelet rich plasma for 180 minutes

Fig. 3 Surface treatment and thrombogenicity of thin film nitinol

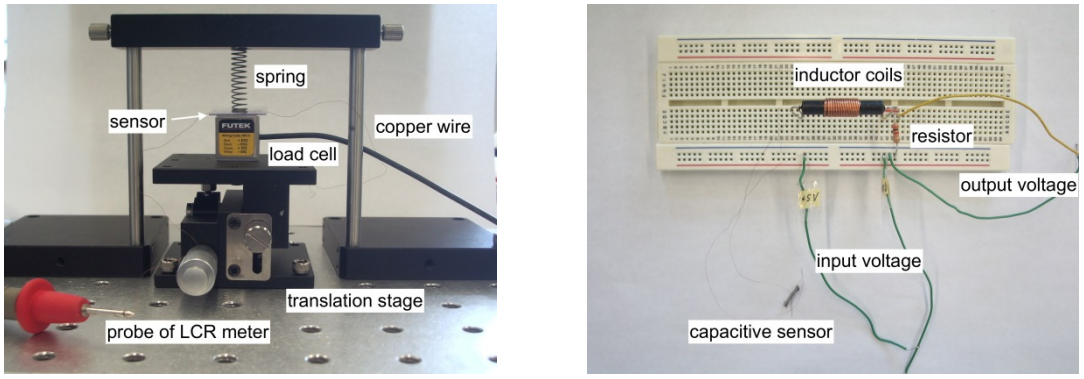

(a) Testing setup for a mechanical compression test (b) Circuit for the resonant frequency measurement

Fig. 4 Experimental setup for a mechanical compression test with the prototype flow sensor

The corresponding RF signals according to the increased compression force was also measured using the circuit shown in Fig. 4(b). The inductance of the coils is 0.1 mF and the resistance of the resistor is 3 kΩ. The input sine-wave signal was supplied by the function generator (Tektronix, PA) with increasing frequency and the output voltage was measured by the oscilloscope (Tektronix, PA). The frequency with the maximal output voltage peak amplitude was identified as the RF with the applied compression force.

4. Results and discussions

4.1 Modeling

4.1.1 Finite Element Modeling (FEM)

The deformation results were calculated in ANSYS Workbench 15.0 Static Structural. Fig. 5(a) shows the simplified model used in finite element analysis and the polyurethane layer was sandwiched between two TFN plates. The length, width and thickness of the polyurethane layer are denoted as L, W and T, respectively and the thickness of the TFN plates is denoted as t. A compression force of 0.6 N was applied normal to the electrode plate and the bottom layer was fixed in ideal case. Young's modulus for polyurethane is 100 kPa and Poisson's ratio is 0.49. For TFN, Young's Modulus is 33 GPa and Poisson's ratio is 0.3. It also shows the cross-sectional view of the model and TFN layer has a thickness of 5 μm. The directional deformation (defined as the deformation along the force direction) with increasing Young's Modulus of the elastomer layer from 100 kPa, 500 kPa, 1 MPa to 2 MPa is shown in Fig. 5(b). The directional deformation with applied compression force was estimated by averaging the maximal and minimum directional deformation in the top electrode layer. We can see that the directional deformation is inversely proportional to the Young's Modulus of the elastomer layer. Therefore, the elastomer material with a lower Young's Modulus leads to a larger deformation and sensor sensitivity. Fig. 5(c) shows the directional deformation with increasing length/width ratio of the TFN plates from 1 (L=6 mm:W=6 mm), 2.25 (L=9 mm:W=4 mm), 4 (L=12 mm:W=3 mm), 9 (L=18 mm:W=2 mm) to 36 (L=36 mm:W=1 mm) with constant areas ($L\times W$=36 mm^2). It appears that increasing the length/width ratio will increase the deformation of the elastomer with applied force. Therefore, the length should be increased and width should be decreased in order to improve the sensor sensitivity. For the increasing thickness of polyurethane layer from 0.5 mm, 0.8 mm, 1 mm and 1.5 mm to 2 mm, we calculated directional deformation over square of original thickness described in Eq. (6) since the original capacitance also changed with varying thickness and the results are shown in Fig. 5(d). Fig. 5(d) shows that decreasing the thickness of the elastomer (or gap between two electrode layers) leads to a decrease in elastomer deformation, but an increase in the capacitance as well as sensor sensitivity. Also note that decreasing the thickness of elastomer layer will improve the sensor sensitivity dramatically.

We also calculated the capacitance using the Eq. (1) with increasing compression force from 2 g (~0.02 N) to 60 g (~0.6 N) for prototype sensor with dimensions L=6 mm, W=6 mm, T=0.8 mm; L=12 mm, W=3 mm, T=0.5 mm and L=12 mm, W=3 mm, T=0.8 mm in Fig. 6. The linear regression line was fitted for each sensor and all of the cases have $R^2\approx1$, which shows a strong linear relationship between the resultant capacitance and applied compression force. Therefore, it proves the functionality of our proposed sandwich structure as a flow (force) sensor. Also we could compare the sensitivity defined as the capacitance change per gram compression force (i.e.,

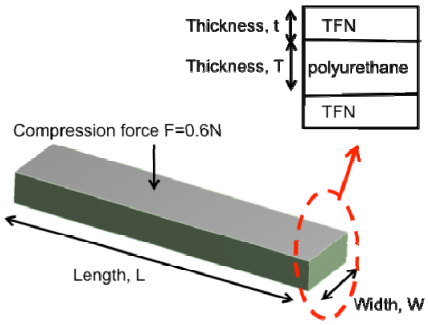

(a) Geometry model of a TFN sensor

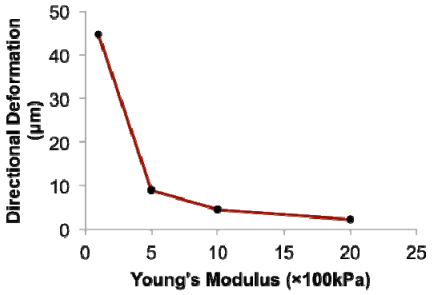

(b) Directional deformation as a function of Young's modulus of the polyurethane layer

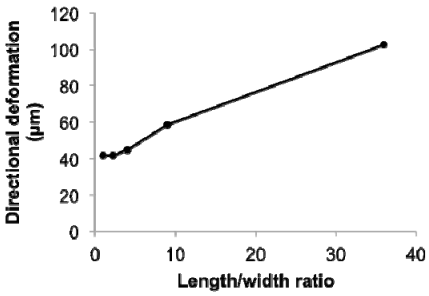

(c) Directional deformation as a function of length/width ratio of the sensor

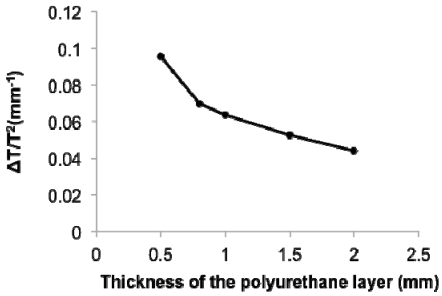

(d) Directional deformation as a function of the thickness of the polyurethane layer

Fig. 5 FEM results for directional deformation of a TFN sensor

slope of the fitted line) for three prototype sensors. In Fig. 6(a), the slope is 0.00229 pF/g, the slope in Fig. 6(b) is 0.00336 pF/g and in Fig. 6(c) is 0.00248 pF/g. It shows that increasing the length/width ratio from 1 (6 mm: 6 mm) to 4 (12 mm: 3 mm) leads to an increase of capacitance change from 0.00229 pF/g to 0.00248 pF/g and decreasing the thickness from 0.8 mm to 0.5 mm increases the capacitance from 0.00248 pF/g to 0.00336 pF/g. The results agree well with the analytical calculation, which shows the sensor sensitivity will be improved by increasing the length/width ratio and decreasing the thickness of the elastomer layer. Areas for further development include the device size that provides ultra-low profile using stretchable nanomembranes (Fan *et al*. 2014) to be directly embedded into a stent without disrupting intra-aneurysmal flow and the design configuration that offers wireless monitoring of hemodynamics through battery-less, inductive coupling based data transmission (Huang *et al*. 2014).

4.1.2 Computational fluid dynamics (CFD) modeling

The CFD calculations were performed in ANSYS Fluent 15.0 and Fig. 7(a) shows the geometry of aneurysm model used in the calculations. The aneurysm was simplified as a sphere (aneurysm sac) with diameter 8 mm attached on the wall of a cylindrical tube (parent vessel) with length of 2 cm and diameter of 4 mm. The length of the neck was 5.5 mm, which was defined as the distance between two contact points in the cylindrical tube. The density and the viscosity of the blood flow were 1050 kg/m^3 and 3.5 cP. Finally, the velocity of the blood flow at the inlet was 0.5 m/s and the pressure at the outlet was set as 0. The symmetry was also used and only half of the aneurysm

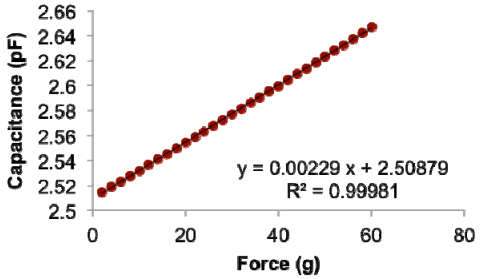

(a) Calculated capacitance change for sensor with dimension L=6 mm, W=6 mm, T=0.8 mm

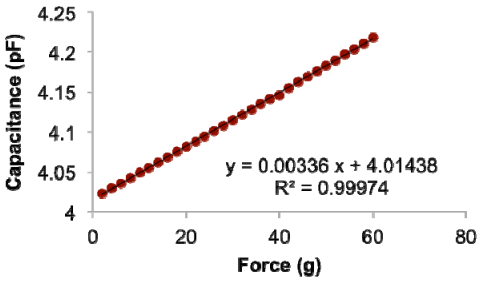

(b) Calculated capacitance change for sensor with dimension L=12 mm, W=3 mm, T=0.5 mm

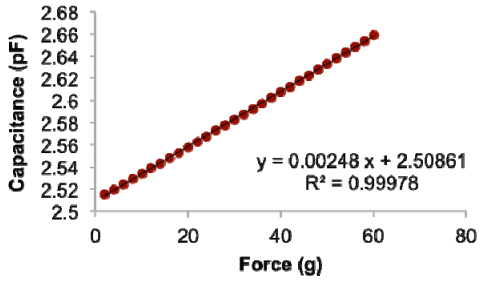

(c) Calculated capacitance change for sensor with dimension L=12 mm, W=3 mm, T=0.8 mm

Fig. 6 Calculated capacitance change of three different sensors with varying compression forces

model was analyzed in the CFD calculations. Fig. 7(b) and (c) show the flow velocity distributions on the symmetry plane in the whole aneurysm region, including the parent vessel and aneurysm sac. The flow in the aneurysm sac region adopts the counterclockwise fashion, which means that the inlet flow will enter the sac at the distal end and exit at the proximal end. Also note that there are numerous small vortices within the sac, showing a complex flow pattern. Fig. 7(c) also shows the flow magnitude distributions, with the maximal velocity (in the range of [0.102, 0.134] m/s) at the aneurysm entrance and minimal velocity (in the range of [0.0029, 0.0036] m/s) at the dome. This calculation results match well with previous experiment results using particle image velocimetry systems (Chun *et al*. 2011). Another important factor in the aneurysm region is pressure. Figs. 7(d) and (e) show the static pressure and dynamic pressure contour plots in the symmetry plane. It can be seen that the static pressure in the sac region is similar to the parent vessel and the dynamic pressure is reduced from the aneurysm entrance to the dome due to the velocity decrease. It confirms the hypothesis that static pressure is uniformly distributed among the sac region while the dynamic pressure (or flow velocity) varied and should be monitored to assess hemodynamic quiescence within the aneurysm sac.

4.2 Compression test results

A set of prototype sensors was tested using the compression test system. Fig. 8(a) shows one prototype sensor with the length (L: 12 mm), width (W: 3 mm) and thickness (T: 0.5 mm). Prototype sensor 1 has the following dimensions: L:W:T=6 mm:6 mm:0.8 mm, and the measured capacitance changes with increasing compression force from 5 g (~0.05 N) to 60 g (~0.6 N).

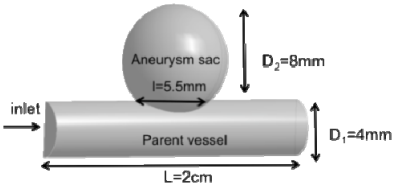

(a) Geometry model

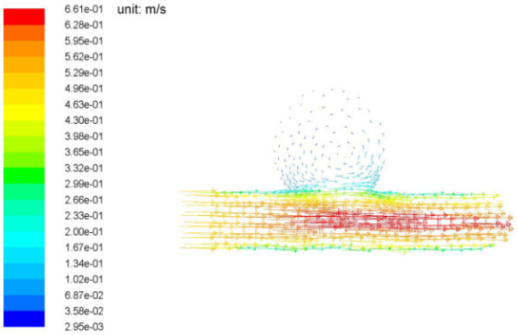

(b) Velocity vector on the symmetry plane in the aneurysm model

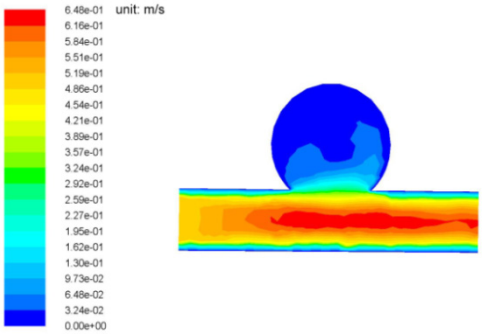

(c) Velocity contour on the symmetry plane in the aneurysm model

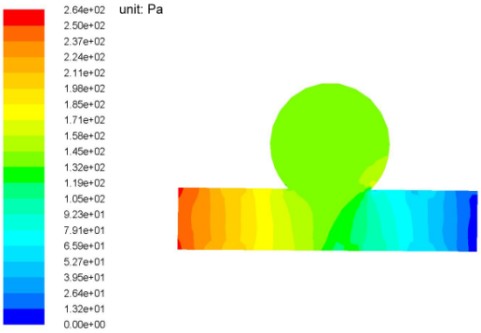

(d) Static pressure contour on the symmetry plane in the aneurysm model

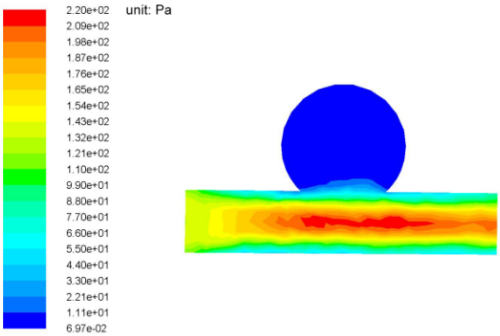

(e) Dynamic pressure contour on the symmetry plane in the aneurysm model

Fig. 7 CFD results for the blood flow profiles with an aneurysm sac

Prototype sensor 2 has the dimensions: L:W:T=12 mm:3 mm:0.5 mm and prototype sensor 3 has the dimensions: L:W:T=12 mm:3 mm:0.8 mm. We gradually elevated the height of the translation stage and the corresponding capacitance change was measured. Then, the exported data points were filtered by calculating Cook's D statistics (Matlab) to remove the outliers during the measurement. Fig. 8(b) plots the capacitance versus the compression force and a linear regression equation was calculated with R^2=0.50672. The sensitivity of the sensor (i.e., slope of the linear regression equation) is 0.00150 pF/g. Figs. 8(c) and (d) plot the capacitance versus compression force with R^2=0.71392, R^2=0.76725, respectively. The sensitivity for sensor 2 and sensor 3 is 0.00323 pF/g and 0.00305 pF/g, respectively. The results show that sensor 3 has higher sensitivity than sensor 1. It confirms the analysis that increasing the length/width ratio enhances the sensor sensitivity. In addition, sensor 2 shows higher sensitivity than sensor 3, which confirms that

thinner elastomer decreases the deformation, but enhances the sensor sensitivity. Overall, the experimental results match well with the theoretical calculations (Fig. 5). Higher capacitance in compression tests might be caused by the parasite capacitance induced by copper wires and other environmental parameters.

4.3 RF measurement

The resonant frequency of the capacitive sensor (prototype sensor 3) coupled with an inductor coil was measured using the circuit (section 3.2). The compression force was gradually increased from 0 g to 200 g (~2 N) and the corresponding resonant frequency was measured from oscilloscope connected to the output end. Fig. 9(a) shows that the resonant frequency decreased from 12.7 MHz to 12.48 MHz, indicating a 0.22 MHz with a 2 N compression force applied on the sensor. The theoretical resonant frequency with increasing compression force from 0 g to 50 g (~0.5 N) was also plotted in Fig. 9(b). The resonant frequency, dropped from 9.35 MHz to ~9 MHz indicates a resonant frequency shift due to the compression force (0.5 N). This resonant frequency shift is larger than the experimental results. The discrepancy between the experiment and calculation could be caused by the parasite capacitance and inductance in the testing circuit.

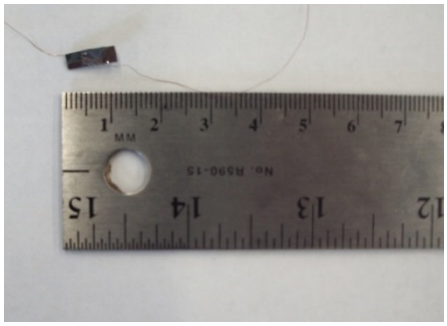

(a) A prototype flow sensor connected through copper wires

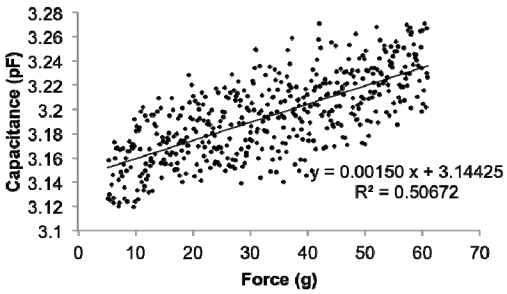

(b) Measured capacitance as a function of an applied compression force for the prototype sensor 1 with length (*L*):width (*W*):thickness (*T*) of the elastomer layer=6 mm:6 mm:0.8 mm

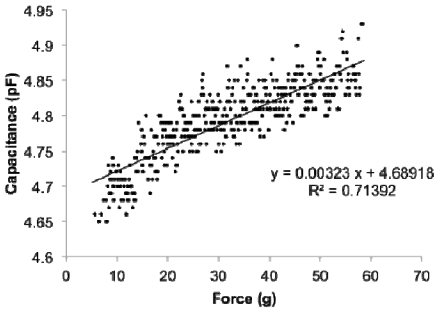

(c) Measured capacitance as a function of an applied compression force for the prototype sensor 2 with length (*L*):width (*W*):thickness (*T*) of the elastomer layer=12 mm:3 mm:0.5 mm

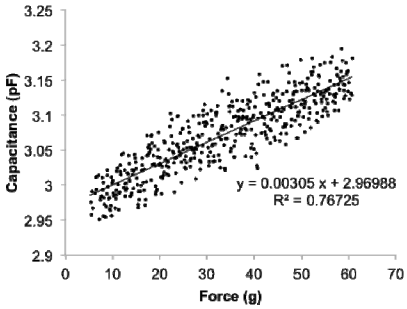

(d) Measured capacitance as a function of an applied compression force for the prototype sensor 3 with length (*L*):width (*W*):thickness (*T*) of the elastomer layer=12 mm:3 mm:0.8 mm

Fig. 8 Compression test results

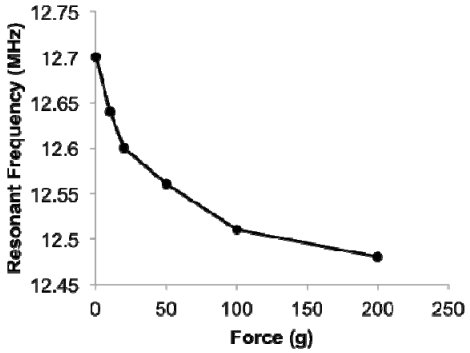

(a) Measured resonant frequency of the prototype sensor with increasing compression force from 0 g to 200 g (~2 N)

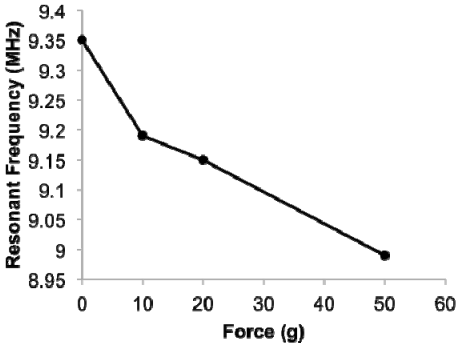

(b) Calculated resonant frequency of the prototype sensor with increasing compression force from 0 g to 50 g (~0.5 N)

Fig. 9 Results of measured RF change according to a compression force

5. Conclusions

In summary, a microfabricated, low-profile flow sensor demonstrated the capability to monitor *in vitro* hemodynamics within the aneurysm sac. The prototype device was designed as a parallel capacitor including two electrode layers (TFN) that enclosed an ultra-thin dielectric elastomer (polyurethane) in the middle. A finite element modeling optimized the sensor design and the analysis of computational fluid dynamics provided flow velocity profiles within the aneurysm sac. The experimental results demonstrated that increased ratio of length/width and thickness of the elastomer layer enhanced the sensor sensitivity. The computational analysis determined that the optimal location of the sensor was near the neck regions with the maximal flow velocity. The feasibility of the fabricated flow sensor was verified through the compression test and resonant frequency measurements. Further development of the flow sensor includes an *in vitro* testing of the sensor in an aneurysm model with a pulsatile pump and the integration of wireless powering and telecommunication systems.

Acknowledgments

The authors gratefully appreciate funding from the American Heart Association (award number 14BGIA18690043) and Central Research Development Fund at the University of Pittsburgh. W.-H.Y. acknowledges startup funding from the School of Engineering, Virginia Commonwealth University.

References

Babiker, M.H., Gonzalez, L.F., Albuquerque, F., Collins, D., Elvikis, A. and Frakes, D.H. (2010), "Quantitative effects of coil packing density on cerebral aneurysm fluid dynamics: an in vitro steady flow study", *Ann. Biomed. Eng.*, **38**(7), 2293-2301.

Brisman, J.L., Song, J.K. and Newell, D.W. (2006), "Cerebral aneurysms", *New England J. Med.*, **355**(9),

928-939.
Boecher-Schwarz, H.G., Ringel, K., Kopacz, L., Heimann, A. and Kempski, O. (2000), "Ex vivo study of the physical effect of coils on pressure and flow dynamics in experimental aneurysms", *Am. J. Neuroradiol.*, **21**(8), 1532-1536.
Canton, G., Levy, D.I. and Lasheras, J.C. (2005), "Changes in the intraaneurysmal pressure due to hydrocoil embolization", *Am. J. Neuroradiol.*, **26**(4), 904-907.
Chun, Y., Hur, S.C., Kealey, C.P., Levi, D.S., Mohanchandra, K.P., Carlo, D.D., Eldredge, J.D., Vinuela, F. and Carman, G.P. (2011), "Intra-aneurysmal flow reductions in a thin film nitinol flow diverter", *Smart Mater. Struct.*, **20**(5), 055021.
Chun, Y., Levi, D.S., Mohanchandra, K. and Carman, G.P. (2009), "Superhydrophilic surface treatment for thin film nitinol vascular applications", *Mater. Sci. Eng.: C*, **29**(8), 2436-2441.
Dias, N.V., Ivancev, K., Malina, M., Hinnen, J.W., Visser, M., Lindblad, B. and Sonesson, B. (2004), "Direct intra-aneurysm sac pressure measurement using tip-pressure sensors: in vivo and in vitro evaluation", *J. Vas. Surg.*, **40**(4), 711-716.
Huang, X., Liu, Y., Cheng, H., Shin, W., Fan, J., Liu, Z., Lu, C., Kong, G., Chen, K., Patnaik, D., Lee, S., Hage-Ali, S., Huang, Y. and Rogers, J.A. (2014), "Materials and designs for wireless epidermal sensors of hydration and strain", *Adv. Func. Mater.*, **24**(25), 3846.
Ellozy, S.H., Carroccio, A., Lookstein, R.A., Minor, M.E., Sheahan, C.M., Juta, J., Cha, A., Valenzuela, R., Addis, M.D., Jacobs, T.S. *et al*. (2004), "First experience in human beings with a permanently implantable intrasac pressure transducer for monitoring endovascular repair of abdominal aortic aneurysms", *J. Vas. Surg.*, **40**(3), 405-412.
Fan, J., Yeo, W.H., Su, Y., Hattori, Y., Lee, W., Jung, S., Cheng, H., Zhang, Y., Liu, Z., Falgout,L., Bajema, M., Coleman, T., Gregoire, D., Larson, R., Huang, Y. and Rogers, J. A. (2014), "Fractal design concepts for stretchable electronics", *Nature Commun.*, **5**, 3266.
Go, A.S., Moza_arian, D., Roger, V.L., Benjamin, E.J., Berry, J.D., Borden, W.B., Bravata, D.M., Dai, S., Ford, E.S., Fox, C.S. *et al*. (2013), "Heart disease and stroke statistics-2013 update: a report from the American Heart Association", *Circulation*, **127**(1), e6-e245.
Groden, C., Laudan, J., Gatchell, S. and Zeumer, H. (2001), "Three-dimensional pulsatile flow simulation before and after endovascular coil embolization of a terminal cerebral aneurysm", *J. Cerebral Blood Flow Metabol.*, **21**(12), 1464-1471.
Juvela, S., Poussa, K., Lehto, H. and Porras, M. (2013), "Natural history of unruptured intracranial aneurysms a long-term follow-up study", *Stroke*, **44**(9), 2414-2421.
Kenichi, T. and Gianchandani, Y.B. (2008), "A micromachined capacitive pressure sensor using a cavity-less structure with bulk-metal/elastomer layers and its wireless telemetry application", *Sensors*, **8**(4), 2317-2330.
Lam, A.K., Ko, M.W., Leung, L.K., Kwok, J.C., Yuen, M.M. and Lam, D.C., "Characterization of pressure reduction in coil-filled aneurysm under flow of human blood with and without anti-coagulant", *In Engineering in Medicine and Biology Society (EMBC), 2013 35th Annual International Conference of the IEEE*.
Molyneux, A.J., Kerr, R.S., Yu, L.M., Clarke, M., Sneade, M., Yarnold, J.A. and Sandercock, P. (2005), "International subarachnoid aneurysm trial (ISAT) of neurosurgical clipping versus endovascular coiling in 2143 patients with ruptured intracranial aneurysms: a randomised comparison of e_ects on survival, dependency, seizures, rebleeding, subgroups, and aneurysm occlusion", *Lancet*, **366**(9488), 809-817.
Morales, H.G., Kim, M., Villa-Uriol, M.C., Diaz, E.V. and Frangi, A.F. (2009), "Inuence of coil packing rate and configuration on intracranial aneurysm hemodynamics", *In World Congress on Medical Physics and Biomedical Engineering*, Munich, Germany.
Ohki, T., Ouriel, K., Silveira, P.G., Katzen, B., White, R., Criado, F. and Diethrich, E. (2007), "Initial results of wireless pressure sensing for endovascular aneurysm repair: the APEX trial-acute pressure measurement to confirm aneurysm sac exclusion", *J. Vas. Surg.*, **45**(2), 236-242.
Raymond, J., Guilbert, F., Weill, A., Georganos, S.A., Juravsky, L., Lambert, A., Lamoureux, J., Chagnon, M. and Roy, D. (2003), "Long-term angiographic recurrences after selective endovascular treatment of

aneurysms with detachable coils", *Stroke*, **34**(6), 1398-1403.
Rinkel, G.J., Djibuti, M., Algra, A. and Van Gijn, J. (1998), "Prevalence and risk of rupture of intracranial aneurysms a systematic review", *Stroke*, **29**(1), 251-256.
Sorteberg, A., Sorteberg, W., Turk, A.S., Rappe, A., Nakstad, P.H. and Strother, C.M. (2001), "Effect of Guglielmi detachable coil placement on intraaneurysmal pressure: experimental study in canines", *Am. J. Neuroradiol.*, **22**(9), 1750-1756.
Szycher, M. (2012), *Szycher's Handbook of Polyurethanes*, Second Edition, CRC Press.
Tulloch, A.W., Chun, Y., Levi, D.S., Mohanchandra, K.P., Carman, G.P., Lawrence, P.F. and Rigberg, D. A. (2011), "Super hydrophilic thin film nitinol demonstrates reduced platelet adhesion compared with commercially available endograft materials", *J. Surg. Res.*, **171**(1), 317-322.
Vlak, M.H., Algra, A., Brandenburg, R. and Rinkel, G.J. (2011), "Prevalence of unruptured intracranial aneurysms, with emphasis on sex, age, comorbidity, country, and time period: a systematic review and meta-analysis", *Lancet Neurol.*, **10**(7), 626-636.
Wardlaw, J.M. and White, P.M. (2000), "The detection and management of unruptured intracranial aneurysms", *Brain*, **123**(2), 205-221.

YC